

# High-throughput calculations of magnetic topological materials

<https://doi.org/10.1038/s41586-020-2837-0>

Received: 27 January 2020

Accepted: 24 August 2020

Published online: 28 October 2020

 Check for updates

Yuanfeng Xu<sup>1</sup>, Luis Elcoro<sup>2</sup>, Zhi-Da Song<sup>3</sup>, Benjamin J. Wieder<sup>3,4,5</sup>, M. G. Vergniory<sup>6,7</sup>, Nicolas Regnault<sup>3,8</sup>, Yulin Chen<sup>9,10,11,12</sup>, Claudia Felser<sup>13,14</sup> & B. Andrei Bernevig<sup>1,3,15</sup>✉

The discoveries of intrinsically magnetic topological materials, including semimetals with a large anomalous Hall effect and axion insulators<sup>1–3</sup>, have directed fundamental research in solid-state materials. Topological quantum chemistry<sup>4</sup> has enabled the understanding of and the search for paramagnetic topological materials<sup>5,6</sup>. Using magnetic topological indices obtained from magnetic topological quantum chemistry (MTQC)<sup>7</sup>, here we perform a high-throughput search for magnetic topological materials based on first-principles calculations. We use as our starting point the Magnetic Materials Database on the Bilbao Crystallographic Server, which contains more than 549 magnetic compounds with magnetic structures deduced from neutron-scattering experiments, and identify 130 enforced semimetals (for which the band crossings are implied by symmetry eigenvalues), and topological insulators. For each compound, we perform complete electronic structure calculations, which include complete topological phase diagrams using different values of the Hubbard potential. Using a custom code to find the magnetic co-representations of all bands in all magnetic space groups, we generate data to be fed into the algorithm of MTQC to determine the topology of each magnetic material. Several of these materials display previously unknown topological phases, including symmetry-indicated magnetic semimetals, three-dimensional anomalous Hall insulators and higher-order magnetic semimetals. We analyse topological trends in the materials under varying interactions: 60 per cent of the 130 topological materials have topologies sensitive to interactions, and the others have stable topologies under varying interactions. We provide a materials database for future experimental studies and open-source code for diagnosing topologies of magnetic materials.

Non-magnetic topological materials have dominated topological physics for the past two decades. Research in this field has led to a rapid succession of theoretical and experimental discoveries; notable examples include the theoretical prediction of topological insulators in two<sup>8,9</sup> and three spatial dimensions<sup>10</sup>, topological crystalline insulators<sup>11</sup>, Dirac and Weyl semimetals<sup>12–18</sup>, and non-symmorphic topological insulators and semimetals<sup>19–23</sup>. Although topological materials were once believed to be rare and esoteric, recent advances in nonmagnetic topological materials have found that topological insulators and enforced semimetals are much more prevalent than initially thought. In 2017, topological quantum chemistry and the equivalent method of symmetry-based indicators provided a description of the universal global properties of all possible atomic limit band structures in all non-magnetic symmetry groups, in real and momentum space<sup>4,24–27</sup>. This allowed a classification

of the non-magnetic, non-trivial (topological) band structures, using high-throughput methods that have changed our understanding of the number of naturally occurring topological materials. About 40%–50% of all non-magnetic materials can be classified as topological at the Fermi level<sup>5,6,28</sup>, providing a ‘periodic table’ of topological materials.

These breakthroughs in non-magnetic materials have not yet been matched by similar advances in magnetic compounds, owing to a multitude of challenges. First, although a method for classifying band topology in the 1,651 magnetic and nonmagnetic space groups was recently introduced<sup>29</sup>, there still does not exist a theory similar to topological quantum chemistry or equivalent methods<sup>4,24–27</sup> with which the indicator groups in ref. <sup>29</sup> can be linked to topological (anomalous) surface (and hinge) states. Second, a full classification of the magnetic co-representations and compatibility relations has not yet been tabulated. Third, code to

<sup>1</sup>Max Planck Institute of Microstructure Physics, Halle, Germany. <sup>2</sup>Department of Condensed Matter Physics, University of the Basque Country UPV/EHU, Bilbao, Spain. <sup>3</sup>Department of Physics, Princeton University, Princeton, NJ, USA. <sup>4</sup>Department of Physics, Massachusetts Institute of Technology, Cambridge, MA, USA. <sup>5</sup>Department of Physics, Northeastern University, Boston, MA, USA. <sup>6</sup>Donostia International Physics Center, Donostia/San Sebastian, Spain. <sup>7</sup>IKERBASQUE, Basque Foundation for Science, Bilbao, Spain. <sup>8</sup>Laboratoire de Physique de l'École normale supérieure, ENS, Université PSL, CNRS, Sorbonne Université, Université Paris-Diderot, Sorbonne Paris Cité, Paris, France. <sup>9</sup>School of Physical Science and Technology, ShanghaiTech University, Shanghai, China. <sup>10</sup>ShanghaiTech Laboratory for Topological Physics, Shanghai, China. <sup>11</sup>Clarendon Laboratory, Department of Physics, University of Oxford, Oxford, UK. <sup>12</sup>State Key Laboratory of Low Dimensional Quantum Physics, Department of Physics and Collaborative Innovation Center of Quantum Matter, Tsinghua University, Beijing, China. <sup>13</sup>Max Planck Institute for Chemical Physics of Solids, Dresden, Germany. <sup>14</sup>Center for Nanoscale Systems, Faculty of Arts and Science, Harvard University, Cambridge, MA, USA. <sup>15</sup>Physics Department, Freie Universität Berlin, Berlin, Germany. ✉e-mail: bernevig@princeton.edu

**Table 1 | Topological categories vary with  $U$**

MSG	Topological insulators/SISMs			Enforced semimetals/ESFDs			MSG	Topological insulators/SISMs			Enforced semimetals/ESFDs			MSG	Topological insulators/SISMs			Enforced semimetals/ESFDs		
	$U=0$	$U=2$	$U=4$	$U=0$	$U=2$	$U=4$		$U=0$	$U=2$	$U=4$	$U=0$	$U=2$	$U=4$		$U=0$	$U=2$	$U=4$	$U=0$	$U=2$	$U=4$
2.7	1	0	1	0	1	0	62.447	0	1	0	1	0	0	129.416	0	0	1	0	1	0
4.7	0	1	0	0	0	0	62.450	2	2	1	2	1	2	130.432	0	1	0	1	0	1
11.54	1	0	1	0	0	0	63.462	0	2	0	2	0	2	132.456	0	1	0	1	0	1
11.57	1	0	0	0	0	0	63.463	0	1	0	1	0	1	134.481	3	0	1	1	2	0
12.62	2	0	1	0	1	0	63.464	1	1	1	1	0	1	135.492	0	2	0	2	0	2
12.63	0	0	0	0	0	0	63.466	0	0	2	0	1	1	138.528	1	0	1	0	1	0
13.73	2	0	2	0	1	0	63.467	0	0	0	0	1	0	139.536	0	1	0	1	0	1
14.75	0	1	0	0	0	0	64.480	3	0	2	0	0	1	139.537	0	1	0	1	0	1
14.80	1	0	0	0	0	0	65.486	0	0	0	1	0	1	140.550	0	2	1	2	1	2
15.89	2	1	3	0	3	0	65.489	1	0	0	1	0	1	141.556	0	1	0	0	1	0
15.90	4	0	0	0	0	0	67.510	0	0	1	0	0	0	141.557	1	4	0	1	0	1
18.22	0	1	0	0	0	0	70.530	0	1	0	0	0	0	148.19	0	1	0	1	0	1
33.154	0	1	0	0	0	0	71.536	0	1	0	1	0	1	155.48	0	0	0	0	0	1
36.178	0	0	0	0	0	1	73.553	1	0	1	0	1	0	161.69	0	1	0	1	0	0
38.191	0	1	0	0	0	0	74.559	0	1	0	1	0	1	161.71	0	2	0	2	0	0
49.270	0	1	0	1	0	1	85.59	0	1	0	1	0	1	165.95	0	1	0	0	0	0
49.273	0	1	1	0	1	0	88.81	0	1	0	0	0	0	166.101	1	3	0	3	1	2
51.295	0	1	0	1	0	1	92.114	0	1	0	1	0	1	166.97	0	1	0	1	0	1
51.298	0	1	0	1	0	1	107.231	0	0	0	1	0	1	167.108	0	1	0	0	0	0
53.334	0	0	0	0	1	0	114.282	0	1	0	0	0	0	185.201	1	0	0	0	0	0
57.391	1	0	1	0	1	0	123.345	0	1	0	1	0	1	192.252	0	2	0	2	0	2
58.398	0	1	0	0	0	0	124.360	1	3	0	4	0	4	194.268	0	0	0	0	0	1
58.399	0	2	0	2	0	2	125.373	0	1	0	1	0	1	205.33	1	0	0	0	0	0
59.407	0	1	0	0	0	0	126.386	0	1	0	1	0	1	222.103	0	1	0	1	0	1
59.416	0	0	1	0	1	0	127.394	1	1	1	1	1	1	224.113	2	1	2	0	2	0
60.431	1	0	0	0	0	0	127.397	0	1	0	1	0	1	227.131	0	1	0	0	0	0
61.439	0	0	1	0	0	0	128.408	0	1	0	1	0	1	228.139	2	1	0	3	0	3
62.441	0	3	0	0	0	0	128.410	0	4	0	4	0	4	Total	38	27	24	73	58	57

Shown are the number of magnetic topological insulators/SISMs and enforced semimetals/ESFDs in each MSG for different values of the Hubbard interaction  $U = 0$  eV, 2 eV and 4 eV. For  $U = 0$ , there are 38 topological insulators/SISMs and 73 enforced semimetals/ESFDs in total. For  $U = 2$  eV, the numbers of topological insulators/SISMs and enforced semimetals/ESFDs decrease to 27 and 58, respectively. For  $U = 4$  eV, the numbers of topological insulators/SISMs and enforced semimetals/ESFDs decrease to 24 and 57, respectively. Choosing the value of  $U$  for each material for which the magnetic moments calculated ab initio lie closest to their experimentally measured values, there are 29 topological insulators/SISMs and 62 enforced semimetals/ESFDs.

compute the magnetic co-representations from ab initio band structures does not exist. Fourth, and finally, even if all the above were available, the ab initio calculation of magnetic compounds is notoriously inaccurate for complicated magnetic structures beyond ferromagnets. Specifically, unless the magnetic structure of a material is known a priori, then the ab initio calculation will probably converge to a misleading ground state. This has meant that the number of accurately predicted magnetic topological materials is less than ten<sup>1–3,30–39</sup>.

In the present work and in ref. <sup>7</sup>, we present substantial advances towards solving all of the above challenges—which we have made freely available to the public on internet repositories (<https://www.cryst.ehu.es/cryst/checktopologicalmagmat>)—covering four years of our work on the subject, and over 70 years<sup>40</sup> of research on the group theory, symmetry, and topology of magnetic materials. We present a full theory of magnetic indices, co-representations, compatibility relations, code with which to compute the magnetic co-representations directly from ab initio calculations, and we perform full local density approximation (LDA) + Hubbard  $U$  calculations on 549 magnetic structures, which have been accurately tabulated through the careful analysis of neutron-scattering data. We predict several novel magnetic topological phases in real materials, including higher-order magnetic Dirac semimetals with hinge arcs<sup>41</sup>, magnetic chiral crystals with long Fermi arcs,

Dirac semimetals with nodes not related by time-reversal symmetry, Weyl points and nodal lines in non-collinear antiferromagnets, and ideal axion insulators with gapped surface states and chiral hinge modes<sup>42,43</sup>.

### Workflow

Starting from the material database MAGNDATA (<http://webbdcristal.ehu.es/magnadata>) on the Bilbao Crystallographic Server (BCS) (the BCSMD), which contains portable magnetic structure files determined by neutron scattering experiments of more than 707 magnetic structures, we select 549 high-quality magnetic structures for the ab initio calculations. We take the magnetic configurations provided by BCSMD as the initial inputs and then perform ab initio calculations incorporating spin-orbit coupling. LDA +  $U$  are applied for each material with different Hubbard  $U$  parameters to obtain a full phase diagram. Then, we calculate the character tables of the valence bands of each material using the MagVasp2trace package. By feeding the character tables into the machinery of MTQC, that is, the Check Topological Magnetic Mat. (<https://www.cryst.ehu.es/cryst/checktopologicalmagmat>) function on BCS<sup>7</sup>, we identify the corresponding magnetic co-representations (irreps) and classify the materials into different topological categories. Here we define six topological categories:

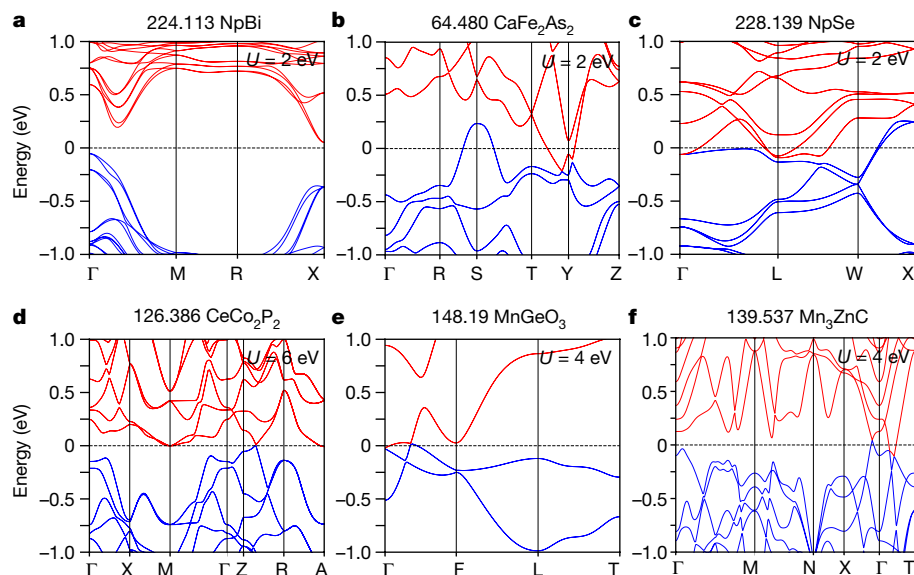


**Fig. 1 | Band structures of the ‘high-quality’ magnetic topological materials predicted by MTQC.** **a, b,** The antiferromagnetic axion topological insulators, NpBi and  $\text{CaFe}_2\text{As}_2$ . Although there are Fermi pockets around S and Y in  $\text{CaFe}_2\text{As}_2$ , the insulating compatibility relations are fully satisfied. We note that there is a small gap (about 5 meV) along the path T–Y; this indicates that the valence bands are well separated from the conduction bands, and thus have a well defined topology. **c,** The antiferromagnetic ESFD NpSe, which has a partially filled fourfold degeneracy at  $\Gamma$ . **d,** The antiferromagnetic nodal-line semimetal  $\text{CeCo}_2\text{P}_2$ . A gapless nodal ring protected by mirror symmetry lies in

the Z–R–A plane. **e,** The antiferromagnetic Dirac semimetal  $\text{MnGeO}_3$ . One of the two Dirac nodes protected by the  $C_3$ -rotation symmetry lies along the high-symmetry line  $\Gamma$ –F. Note that there is a small bandgap at the  $\Gamma$  point. **f,** The non-collinear ferrimagnetic Weyl semimetal  $\text{Mn}_3\text{ZnC}$ . Two Weyl points are pinned to the rotation-invariant line  $\Gamma$ –T by  $C_4$ -rotation symmetry.  $\text{Mn}_3\text{ZnC}$  also hosts nodal lines at the Fermi level  $E_F$ ; we specifically observe five nodal rings protected by the mirror symmetry ( $M_z$ ) in the plane  $k_z = 0$ . The sequential number of each MSG in the BNS setting and the chemical formula of each material are provided on the top of each panel.

(1) Band representation. Insulating phase consistent with atomic insulators.

(2) Enforced semimetal with Fermi degeneracy (ESFD). Semimetal phase with a partially filled degenerate level at a high-symmetry point in the Brillouin zone.

(3) Enforced semimetal. Semimetal phase with un-avoidable level crossings along high-symmetry lines or in high-symmetry planes in the Brillouin zone.

(4) Smith-index semimetal (SISM). Semimetal phase with un-avoidable level crossings at generic points (away from high-symmetry points/lines/planes) in the Brillouin zone.

(5) Stable topological insulator. Insulating phase inconsistent with atomic insulators. The topology (inconsistency with atomic insulators) is stable against being coupled to atomic insulators.

(6) Fragile topological insulator. Insulating phase inconsistent with atomic insulators. The topology is unstable against being coupled to certain atomic insulators.

Further details about BCSMD, the calculation methods, the MagVasp-2trace package, the identification of magnetic irreps, and definitions of the topological categories are given in the Methods.

## Topological phase diagrams

With the irreps successfully identified, we classify 403 magnetic structures with convergent ground states into the six topological categories. We find that there are 130 materials (about 32% of the total) that exhibit nontrivial topology for at least one of the  $U$  values in the phase diagram. We sort these materials into four groups based on their  $U$ -dependence: (1) 50 materials belong to the same topological categories for all values of  $U$ . These are the most robust topological materials. (2) 49 materials, on the other hand, are nontrivial at  $U = 0$  but become trivial when  $U$  is larger than a critical value. (3) 20 materials have non-monotonous dependence on  $U$ : they belong to one topologically nontrivial category at  $U = 0$  and change to a different topologically nontrivial category

at a larger value of  $U$ . (4) Six materials are trivial at  $U = 0$  but become nontrivial after a critical value of  $U$ . The topology of these six interesting materials is thus driven by electron–electron interactions. The materials in this category are:  $\text{CaCo}_2\text{P}_2$ ,  $\text{YbCo}_2\text{Si}_2$ ,  $\text{Ba}_3\text{Co}_5\text{ClO}_{13}$ ,  $\text{U}_2\text{Ni}_2\text{Sn}$ ,  $\text{CeCoGe}_3$ , and  $\text{CeMnAsO}$ . The self-consistent calculations of the remaining five materials do not converge for at least one value of  $U$ , and hence the phase diagrams are not complete. Complete classifications of the converged materials are tabulated in Supplementary Information section 7; the corresponding band structures are given in Supplementary Information section 13. In Table 1, we summarize the total number of topological materials in each magnetic space group (MSG) at different values of  $U$ . We have also provided full topological classifications and band structures of each material on the Topological Magnetic Materials Database (<https://www.topologicalquantumchemistry.fr/magnetic/>).

In the scheme of MTQC, the stable magnetic topological insulators and SISMs are characterized by non-zero stable indices. These indices can be understood as generalizations of the Fu–Kane parity criterion for a three-dimensional topological insulator<sup>44</sup>. A complete table of the stable indices and the index-implied topological invariants, which include (weak) Chern numbers, the axion  $\theta$  angle, and magnetic higher-order topological insulator (HOTI) indices, is given in ref. 7. In Supplementary Information section 8 we present examples of stable indices relevant to the present work, as well as their physical interpretations. Although there are many (1,651) magnetic and nonmagnetic space groups, we find in ref. 7 that the stable indices of all of the MSGs are dependent on minimal indices in the set of the so-called minimal groups. Thus, to determine the stable indices of a material, we first subduce the representation of the MSG formed by the material to a representation of the corresponding minimal group—a subgroup of the MSG on which the indices are dependent. We then calculate the indices in the minimal group. Using this method, we find a tremendous variety of topological phases among the magnetic materials studied in this work, including axion insulators<sup>45–48</sup>, mirror topological crystalline insulators<sup>11</sup>, three-dimensional quantum anomalous Hall insulators, and SISMs.

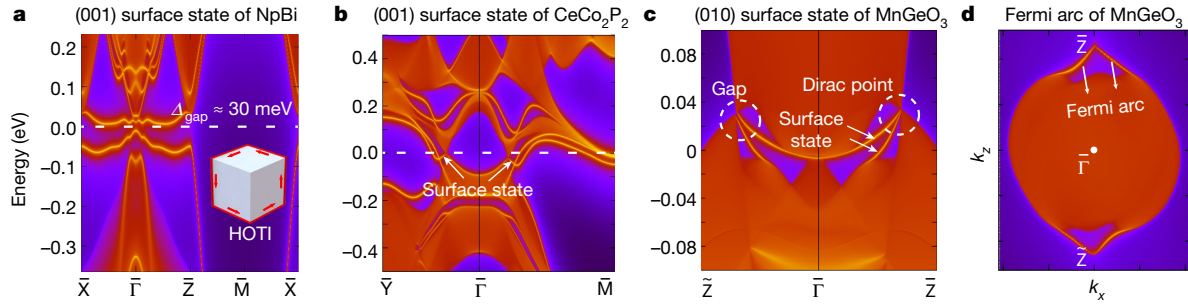


**Fig. 2 | Topological surface states of representative magnetic topological insulator and enforced semimetal phases.** **a**, The (001) surface state of the axion insulator NpBi, which has an energy gap of 30 meV. The inset shows a schematic of the chiral hinge states on a cubic sample. **b**, The (001) surface state of the enforced semimetal CeCo<sub>2</sub>P<sub>2</sub>. The drumhead-like topological surface states connect the projections of the bulk nodal rings. **c**, The (010)

surface state of the enforced semimetal MnGeO<sub>3</sub>. The bulk Dirac point along the  $\bar{\Gamma} - \bar{Z}$  line is protected by  $C_3$  symmetry. However, because time-reversal symmetry is broken, the projected band crossing on  $\bar{\Gamma} - \bar{Z}$  (along  $-k_z$ ) is no longer protected, and is instead weakly gapped. The coordinates of  $\bar{Z}$  and  $\bar{Z}$  on the (010) surface are  $(0, k_z = \pi/c)$  and  $(0, k_z = -\pi/c)$ , respectively. **d**, The surface Fermi arcs connecting the Dirac points on the (010) surface of MnGeO<sub>3</sub>.

A complete table of the topology of all of the magnetic materials studied in this work is provided in Supplementary Information section 8.7.

We additionally discover many ESFD and enforced semimetal materials, in which unavoidable electronic band crossings respectively occur at high-symmetry  $\mathbf{k}$  points or on high-symmetry lines or planes in the Brillouin zone. For each of the ESFD and enforced semimetal magnetic materials, we tabulate the  $\mathbf{k}$  points where unavoidable crossings occur (see Supplementary Information section 9).

We did not discover any examples of magnetic materials for which the entire valence manifold is fragile topological. However, as will be discussed below, we discovered many magnetic materials with well isolated fragile bands in their valence manifolds, thereby providing examples of magnetic fragile bands in real materials.

## High-quality topological materials

We here select several representative ‘high-quality’ topological materials with clean band structures at the Fermi level: NpBi in MSG 224.113 ( $Pn\bar{3}m'$ ) (antiferromagnetic stable topological insulator), CaFe<sub>2</sub>As<sub>2</sub> in MSG 64.480 ( $C_4mca$ ) (antiferromagnetic stable topological insulator), NpSe in MSG 228.139 ( $F_3d\bar{3}c$ ) (antiferromagnetic ESFD), CeCo<sub>2</sub>P<sub>2</sub> in MSG 126.386 ( $PA/nnc$ ) (antiferromagnetic enforced semimetal), MnGeO<sub>3</sub> in MSG 148.19 ( $R\bar{3}'$ ) (antiferromagnetic enforced semimetal) and Mn<sub>3</sub>Zn in MSG 139.537 ( $I4/mmm'$ ) (non-collinear ferrimagnetic enforced semimetal), as shown in Fig. 1. To identify the stable topologies of the antiferrimagnets NpBi and CaFe<sub>2</sub>As<sub>2</sub>, we calculate the stable indices subduced onto MSG 2.4 ( $P\bar{1}$ ), a subgroup of MSG 224.113 ( $Pn\bar{3}m'$ ) and 64.480 ( $C_4mca$ ). The stable indices in MSG 2.4 ( $P\bar{1}$ ) are defined using only parity (inversion) eigenvalues<sup>7,29,42,49–51</sup>:

$$\eta_{4l} = \sum_K n_K^- \bmod 4 \quad (1)$$

$$z_{2l,i} = \sum_{K, K_i=\pi} n_K^- \bmod 2 \quad (2)$$

where  $K$  sums over the eight inversion-invariant momenta, and  $n_K^-$  is the number of occupied states with odd parity eigenvalues at momentum  $K$ .  $z_{2l,i}$  is the parity of the Chern number of the Bloch states in the plane  $k_i = \pi$ . As explained in Supplementary Information section 8,  $\eta_{4l} = 1, 3$  corresponds to Weyl semimetal phases with odd-numbered Weyl points in each half of the Brillouin zone;  $\eta_{4l} = 2$  indicates an axion insulator phase provided that the band structure is fully gapped and the weak Chern numbers in all directions are zero. The inversion eigenvalues of NpBi with  $U = 2$  eV and CaFe<sub>2</sub>As<sub>2</sub> with  $U = 2$  eV are given in Table 2. The corresponding band structures are shown in Fig. 2a and Fig. 2b, respectively. Both NpBi and CaFe<sub>2</sub>As<sub>2</sub> have the indices  $(\eta_{4l}, z_{2l,1}, z_{2l,2}, z_{2l,3}) = (2, 0, 0, 0)$ . As shown in Supplementary Information section 8.7, the  $\eta_{4l}$  index of NpBi is the same for  $U = 0, 2, 4, 6$  eV; whereas the  $\eta_{4l}$  index of CaFe<sub>2</sub>As<sub>2</sub> is 2 for  $U = 0, 1, 2$  eV and 0 for  $U = 3, 4$  eV. We have confirmed that both NpBi and CaFe<sub>2</sub>As<sub>2</sub> have vanishing weak Chern numbers, implying that the  $\eta_{4l} = 2$  phases must be axion insulators.

An axion insulator is defined by a nontrivial  $\theta$  angle, which necessitates a quantized magneto-electric response in the bulk and chiral hinge modes on the boundary<sup>43,45–48</sup>. We have calculated the surface states of NpBi and find that, as expected, the (001) surface is fully gapped (Fig. 2a). Owing to the  $C_3$ -rotation symmetry of the MSG 224.113, the (100) and (010) surfaces are also gapped. Therefore, a cubic sample with terminating surfaces in the (100), (010) and (001) directions, as shown in Fig. 2a, exhibits completely gapped surfaces. However, as an axion insulator, it must exhibit chiral hinge modes when terminated in an inversion-symmetric geometry<sup>42,43</sup>. We predict that the chiral hinge modes exist on the edges shown in Fig. 2a. More details about NpBi are provided in Supplementary Information section 10.1.

Next, we discuss representative examples of magnetic topological semimetals. The antiferrimagnet NpSe with  $U = 2$  eV, 4 eV and 6 eV is an ESFD with a partially filled degenerate band at the  $\Gamma$  point, where the lowest conduction bands and the highest valence bands meet in a fourfold degeneracy (Fig. 1c). The antiferrimagnet CeCo<sub>2</sub>P<sub>2</sub> is an enforced semimetal at all the  $U$  values used in our calculations. For  $U = 0$  eV and 2 eV, we predict CeCo<sub>2</sub>P<sub>2</sub> to be a Dirac semimetal protected by  $C_4$  rotation symmetry. Because the Dirac points in CeCo<sub>2</sub>P<sub>2</sub> lie along

**Table 2 | Parities and topological indices of two magnetic topological insulators**

$\Lambda_o$	(0, 0, 0)	( $\pi$ , 0, 0)	(0, $\pi$ , 0)	( $\pi$ , $\pi$ , 0)	(0, 0, $\pi$ )	( $\pi$ , 0, $\pi$ )	(0, $\pi$ , $\pi$ )	( $\pi$ , $\pi$ , $\pi$ )	$(\eta_{4l}, z_{2l,1}, z_{2l,2}, z_{2l,3})$
NpX	58/22	40/40	40/40	40/40	40/40	40/40	40/40	48/32	(2, 0, 0, 0)
XFe <sub>2</sub> As <sub>2</sub>	50/46	48/48	48/48	52/44	48/48	52/44	52/44	48/48	(2, 0, 0, 0)

Shown are the numbers of occupied bands with odd/even parity eigenvalues at the eight inversion-invariant points ( $\Lambda_o$ ) for the magnetic topological insulators NpX (where X = Sb, Bi) and XFe<sub>2</sub>As<sub>2</sub> (where X = Ca, Ba) with  $U = 2$  eV. The  $\eta_{4l} = 2$  phase corresponds to an axion insulator or Weyl semimetal phase with even pairs of Weyl points at generic locations in the Brillouin zone interior (given vanishing weak Chern numbers), and  $\eta_{4l} = 1, 3$  corresponds to a Weyl semimetal phase with odd number of Weyl points at generic locations within each half of the Brillouin zone. We have confirmed that the weak Chern numbers vanish in NpX and XFe<sub>2</sub>As<sub>2</sub>, implying that both materials are axion insulators.

Table 3 | The magnetic topological materials identified in this work

Categories	Properties	Materials
I-A	Non-collinear manganese compounds	Mn <sub>3</sub> GaC, Mn <sub>3</sub> ZnC, Mn <sub>3</sub> CuN, Mn <sub>3</sub> Sn, Mn <sub>3</sub> Ge, Mn <sub>3</sub> Ir, Mn <sub>3</sub> Pt, Mn <sub>5</sub> Si <sub>3</sub>
I-B	Actinide intermetallic	UNiGa <sub>5</sub> , UPtGa <sub>5</sub> , NpRhGa <sub>5</sub> , NpNiGa <sub>5</sub>
I-C	Rare-earth intermetallic	NdCo <sub>2</sub> , TbCo <sub>2</sub> , NpCo <sub>2</sub> , PrAg DyCu, NdZn, TbMg, NdMg, Nd <sub>5</sub> Si <sub>4</sub> , Nd <sub>5</sub> Ge <sub>4</sub> , Ho <sub>2</sub> RhIn <sub>8</sub> , Er <sub>2</sub> CoGa <sub>8</sub> , Nd <sub>2</sub> RhIn <sub>8</sub> , Tm <sub>2</sub> CoGa <sub>8</sub> , Ho <sub>2</sub> RhIn <sub>8</sub> , DyCo <sub>2</sub> Ga <sub>8</sub> , TbCo <sub>2</sub> Ga <sub>8</sub> , Er <sub>2</sub> Ni <sub>2</sub> In, CeRu <sub>2</sub> Al <sub>10</sub> , Nd <sub>3</sub> Ru <sub>4</sub> Al <sub>12</sub> , Pr <sub>3</sub> Ru <sub>4</sub> Al <sub>12</sub> , ScMn <sub>6</sub> Ge <sub>6</sub> , YFe <sub>4</sub> Ge <sub>4</sub> , LuFe <sub>4</sub> Ge <sub>4</sub> , CeCoGe <sub>3</sub>
II-A	Metallic iron pnictides	LaFeAsO, CaFe <sub>2</sub> As <sub>2</sub> , EuFe <sub>2</sub> As <sub>2</sub> , BaFe <sub>2</sub> As <sub>2</sub> , Fe <sub>2</sub> As, CaFe <sub>4</sub> As <sub>3</sub> , LaCrAsO, Cr <sub>2</sub> As, CrAs, CrN
II-B	Semiconducting manganese pnictides	BaMn <sub>2</sub> As <sub>2</sub> , BaMn <sub>2</sub> Bi <sub>2</sub> , CaMnBi <sub>2</sub> , SrMnBi <sub>2</sub> , CaMn <sub>2</sub> Sb <sub>2</sub> , CuMnAs, CuMnSb, Mn <sub>2</sub> As
II-C	Rare-earth intermetallic compounds with the composition 1:2:2	PrNi <sub>2</sub> Si <sub>2</sub> , YbCo <sub>2</sub> Si <sub>2</sub> , DyCo <sub>2</sub> Si <sub>2</sub> , PrCo <sub>2</sub> P <sub>2</sub> , CeCo <sub>2</sub> P <sub>2</sub> , NdCo <sub>2</sub> P <sub>2</sub> , DyCu <sub>2</sub> Si <sub>2</sub> , CeRh <sub>2</sub> Si <sub>2</sub> , UAu <sub>2</sub> Si <sub>2</sub> , U <sub>2</sub> Pd <sub>2</sub> Sn, U <sub>2</sub> Pd <sub>2</sub> In, U <sub>2</sub> Ni <sub>2</sub> Sn, U <sub>2</sub> Ni <sub>2</sub> In, U <sub>2</sub> Rh <sub>2</sub> Sn
II-D	Rare-earth ternary compounds of the composition 1:1:1	CeMgPb, PrMgPb, NdMgPb, TmMgPb
III-A	Semiconducting actinides/ rare-earth pnictides	HoP, UP, UP <sub>2</sub> , UAs, NpS, NpSe, NpTe, NpSb, NpBi, U <sub>3</sub> As <sub>4</sub> , U <sub>3</sub> P <sub>4</sub>
III-B	Metallic oxides	Ag <sub>2</sub> NiO <sub>2</sub> , AgNiO <sub>2</sub> , Ca <sub>3</sub> Ru <sub>2</sub> O <sub>7</sub> , Double perovskite Sr <sub>3</sub> CoIrO <sub>6</sub>
III-C	Metal-to-insulator transition compounds	NiS <sub>2</sub> , Sr <sub>2</sub> Mn <sub>3</sub> As <sub>2</sub> O <sub>2</sub>
III-D	Semiconducting and insulating oxides, borates, hydroxides, silicates and phosphate	LuFeO <sub>3</sub> , PdNiO <sub>3</sub> , ErVO <sub>3</sub> , DyVO <sub>3</sub> , MnGeO <sub>3</sub> , Tm <sub>2</sub> Mn <sub>2</sub> O <sub>7</sub> , Yb <sub>2</sub> Sn <sub>2</sub> O <sub>7</sub> , Tb <sub>2</sub> Sn <sub>2</sub> O <sub>7</sub> , Ho <sub>2</sub> Ru <sub>2</sub> O <sub>7</sub> , Er <sub>2</sub> Ti <sub>2</sub> O <sub>7</sub> , Tb <sub>2</sub> Ti <sub>2</sub> O <sub>7</sub> , Cd <sub>2</sub> Os <sub>2</sub> O <sub>7</sub> , Ho <sub>2</sub> Ru <sub>2</sub> O <sub>7</sub> , Cr <sub>2</sub> ReO <sub>6</sub> , NiCr <sub>2</sub> O <sub>4</sub> , MnV <sub>2</sub> O <sub>4</sub> , Co <sub>2</sub> SiO <sub>4</sub> , Fe <sub>2</sub> SiO <sub>4</sub> , PrFe <sub>3</sub> (BO <sub>3</sub> ) <sub>4</sub> , KCo <sub>4</sub> (PO <sub>4</sub> ) <sub>3</sub> , CoP <sub>3</sub> , SrMn(VO <sub>4</sub> )(OH), Ba <sub>5</sub> Co <sub>5</sub> ClO <sub>13</sub> , FeI <sub>2</sub>

a high-symmetry line ( $\Gamma$ –Z) whose little group contains  $4mm$ , we see that CeCo<sub>2</sub>P<sub>2</sub> is a higher-order topological semimetal that exhibits flat-band-like higher-order Fermi-arc states on mirror-invariant hinges, analogous to the hinge states recently predicted<sup>41</sup> and experimentally observed<sup>52</sup> in the non-magnetic Dirac semimetal Cd<sub>3</sub>As<sub>2</sub>. For  $U = 4, 6$  eV, CeCo<sub>2</sub>P<sub>2</sub> becomes a nodal ring semimetal protected by the mirror symmetry  $M_z$ . As detailed in Supplementary Information section 10.2, the transition between the two enforced semimetal phases is completed by two successively band inversions at  $\Gamma$  and Z, which removes the Dirac node and creates the nodal ring, respectively. The band structure of the nodal ring semimetal phase at  $U = 6$  eV is plotted in Fig. 1d. The antiferromagnet MnGeO<sub>3</sub> is a  $C_3$ -rotation-protected Dirac semimetal, in which the number of Dirac nodes changes with the value of  $U$ . For  $U = 0$  eV, 1 eV, 3 eV and 4 eV, we predict MnGeO<sub>3</sub> to have two Dirac nodes along the high-symmetry line  $\Gamma$ –F; for  $U = 2$  eV, we observe four Dirac nodes along the same high-symmetry line. In Fig. 1e, we plot the band structure of MnGeO<sub>3</sub> using  $U = 4$  eV. We next predict the non-collinear ferromagnet Mn<sub>3</sub>ZnC to be an enforced semimetal with symmetry-enforced Weyl points coexisting with the Weyl nodal rings (Fig. 1f). Two of the Weyl points in Mn<sub>3</sub>ZnC are pinned by the  $C_4$ -rotation symmetry to the high-symmetry line  $\Gamma$ –T, and we observe five nodal rings protected by the mirror symmetry  $M_z$  in the  $k_z = 0$  plane. In time-reversal-breaking Weyl semimetals, divergent Berry curvature near Weyl points can give rise to a large intrinsic anomalous Hall conductivity<sup>1,2,33,34,53</sup>. We thus expect there to be a large anomalous Hall effect in Mn<sub>3</sub>ZnC. As detailed in Supplementary Information section 10.4, we have specifically calculated the anomalous Hall conductivity of Mn<sub>3</sub>ZnC to be about  $123 \Omega^{-1} \text{cm}^{-1}$ .

The surface states of the enforced semimetals CeCo<sub>2</sub>P<sub>2</sub> and MnGeO<sub>3</sub> are shown in Fig. 2b, c, respectively. Because the bulk states of CeCo<sub>2</sub>P<sub>2</sub> and MnGeO<sub>3</sub> have clean Fermi surfaces, the surface states are well separated from the bulk states, and should be observable in experiments. For the Dirac semimetal MnGeO<sub>3</sub>, we observe a discontinuous Fermi surface (a Fermi arc) on the surface (Fig. 2d). In Supplementary Information section 10, we provide further details of our surface-state calculations.

Consistency with previous work

Our magnetic materials database (<https://www.topologicalquantumchemistry.fr/magnetic>) includes several topological materials that

have previously been reported but whose topology was not known to be protected by symmetry eigenvalues. For example, the non-collinear magnet Mn<sub>3</sub>Sn in MSG 63.463 ( $Cm'cm'$ ) has been reported as a magnetic Weyl semimetal candidate with six pairs of Weyl points<sup>31,54</sup>. In our LDA +  $U$  calculation, for  $U = 0$  eV, 1 eV and 2 eV, we find Mn<sub>3</sub>Sn to be classified instead as a magnetic topological insulator category with the index  $\eta_{41} = 2$ .  $\eta_{41} = 2$  can correspond to several different topological phases (which we emphasize are not all topological insulators): (1) an axion insulator, (2) a three-dimensional quantum anomalous Hall state with even weak Chern number (not determinable from symmetry eigenvalues)<sup>55</sup>, or (3) a Weyl semimetal phase with an even number of Weyl points in half of the Brillouin zone (not determinable from symmetry eigenvalues). Thus our calculations on Mn<sub>3</sub>Sn for  $U = 0$  eV, 1 eV and 2 eV are consistent with the results in refs.<sup>31,54</sup>. We emphasize that if the six Weyl points in half of the Brillouin zone were pairwise annihilated without closing a gap at the inversion-invariant momenta, then the gapped phase would either be an axion insulator or a three-dimensional quantum anomalous Hall state. When  $U$  is further increased to 3 eV and 4 eV, a topological phase transition occurs, driving the  $\eta_{41} = 2$  phase into a gapless enforced semimetal phase.

Chemical categories

In Table 3, we classify the topological magnetic materials predicted by MTQC into three main chemical categories, and 11 sub-categories, through a consideration of their magnetic ions and chemical bonding. Detailed descriptions of each category are given in the Methods. Of the materials listed in Table 3, most antiferromagnetic insulators, which are well studied experimentally in the case of the so-called Mott insulators, appear to be trivial. We observe that most of the materials in Table 3 are identified as topological enforced semimetals or ESFDs, which are defined by small densities of states at the Fermi level, and hence lie chemically at the border between insulators and metals.

Discussion

A large number of the topological materials predicted in this work (see Supplementary Information section 7 for a complete tabulation) can readily be synthesized into single crystals for the exploration of their unusual



physical properties and the confirmation of their topological electronic structures in different phase categories. These include materials with non-trivial topology over the full range of  $U$  values used in our calculations (for example,  $\text{Mn}_3\text{Ge}$ ,  $\text{Mn}_3\text{Sn}$ ,  $\text{Mn}_3\text{Ir}$ ,  $\text{LuFe}_4\text{Ge}_2$  and  $\text{YFe}_4\text{Ge}_2$ ), materials sensitive to  $U$  (for example,  $\text{NdCo}_2$  and  $\text{NdCo}_2\text{P}_2$ ), and interaction-driven topological materials (for example,  $\text{U}_2\text{Ni}_2\text{Sn}$  and  $\text{CeCuGe}_3$ ).

We did not find any examples of materials whose entire valence manifolds are fragile topological. However, it is still possible for well isolated bands within the valence manifold to be fragile topological if they can be expressed as a difference of band representations. We find many examples of energetically well isolated fragile branches among the occupied bands. We tabulate all the fragile branches close to the Fermi level in Supplementary Information section 11.

We emphasize that there also exist topological insulators and topological semimetals (for example, Weyl semimetals) that cannot be diagnosed through symmetry eigenvalues, which in this work are classified as trivial band representations<sup>4</sup>. It is worth mentioning that even the topologically trivial bands may also be interesting if the occupied bands form Wannier functions centred at positions away from the atoms, because a Wannier centre shift in three-dimensional insulators leads to the appearance of topological corner states, like those of quantized ‘quadrupole’ insulators<sup>41</sup>. Topological phases characterized by displaced Wannier functions are known as obstructed atomic limits; we leave their high-throughput calculation for future studies.

## Conclusion

We have performed LDA +  $U$  calculations on 549 existent magnetic structures and have successfully classified 403 using the machinery of MTQC<sup>7</sup>. We find that 130 materials (about 32% of the total) have topological phases as we scan the  $U$  parameter. Our results suggest that a large number of previously synthesized magnetic materials are topologically nontrivial. We highlight several ‘high-quality’ magnetic topological materials that should be experimentally examined for topological response effects and surface (and hinge) states.

## Online content

Any methods, additional references, Nature Research reporting summaries, source data, extended data, supplementary information, acknowledgements, peer review information; details of author contributions and competing interests; and statements of data and code availability are available at <https://doi.org/10.1038/s41586-020-2837-0>.

- Wang, Q. et al. Large intrinsic anomalous Hall effect in half-metallic ferromagnet  $\text{Co}_3\text{Sn}_2\text{S}_2$  with magnetic Weyl fermions. *Nat. Commun.* **9**, 1–8 (2018).
- Liu, E. et al. Giant anomalous Hall effect in a ferromagnetic kagome-lattice semimetal. *Nat. Phys.* **14**, 1125–1131 (2018).
- Otrokov, M. M. et al. Prediction and observation of an antiferromagnetic topological insulator. *Nature* **576**, 416–422 (2019).
- Bradlyn, B. et al. Topological quantum chemistry. *Nature* **547**, 298–305 (2017).
- Vergniory, M. G. et al. A complete catalogue of high-quality topological materials. *Nature* **566**, 480–485 (2019).
- Zhang, T. et al. Catalogue of topological electronic materials. *Nature* **566**, 475–479 (2019).
- Elcoro, L. et al. Magnetic topological quantum chemistry. Preprint at <https://arxiv.org/abs/2010.00598> (2020).
- Kane, C. L. & Mele, E. J.  $Z_2$  topological order and the quantum spin Hall effect. *Phys. Rev. Lett.* **95**, 146802 (2005).
- Bernevig, B. A. & Hughes, T. L. & Zhang, S.-C. Quantum spin Hall effect and topological phase transition in  $\text{HgTe}$  quantum wells. *Science* **314**, 1757–1761 (2006).
- Zhang, H. et al. Topological insulators in  $\text{Bi}_2\text{Se}_3$ ,  $\text{Bi}_2\text{Te}_3$  and  $\text{Sb}_2\text{Te}_3$  with a single Dirac cone on the surface. *Nat. Phys.* **5**, 438–442 (2009).
- Hsieh, T. H. et al. Topological crystalline insulators in the  $\text{SnTe}$  material class. *Nat. Commun.* **3**, 982 (2012).
- Burkov, A. & Balents, L. Weyl semimetal in a topological insulator multilayer. *Phys. Rev. Lett.* **107**, 127205 (2011).
- Wan, X., Ari, M. T., Vishwanath, A. & Savrasov, S. Y. Topological semimetal and Fermi-arc surface states in the electronic structure of pyrochlore iridates. *Phys. Rev. B* **83**, 205101 (2011).
- Xu, G., Weng, H., Wang, Z., Dai, X. & Fang, Z. Chern semimetal and the quantized anomalous Hall effect in  $\text{HgCr}_2\text{Se}_4$ . *Phys. Rev. Lett.* **107**, 186806 (2011).
- Wang, Z. et al. Dirac semimetal and topological phase transitions in  $\text{A}_3\text{Bi}$  ( $\text{A} = \text{Na}, \text{K}, \text{Rb}$ ). *Phys. Rev. B* **85**, 195320 (2012).
- Yang, B.-J. & Nagaosa, N. Classification of stable three-dimensional Dirac semimetals with nontrivial topology. *Nat. Commun.* **5**, 4898 (2014).
- Weng, H., Fang, C., Fang, Z., Bernevig, B. A. & Dai, X. Weyl semimetal phase in noncentrosymmetric transition-metal monophosphides. *Phys. Rev. X* **5**, 011029 (2015).
- Huang, S.-M. et al. A Weyl fermion semimetal with surface Fermi arcs in the transition metal monophosphide  $\text{TaAs}$  class. *Nat. Commun.* **6**, 7373 (2015).
- Young, S. M. et al. Dirac semimetal in three dimensions. *Phys. Rev. Lett.* **108**, 140405 (2012).
- Slager, R.-J., Mesaros, A., Juricic, V. & Zaanen, J. The space group classification of topological band-insulators. *Nat. Phys.* **9**, 98–102 (2013).
- Liu, C.-X., Zhang, R.-X. & VanLeeuwen, B. K. Topological nonsymmorphic crystalline insulators. *Phys. Rev. B* **90**, 085304 (2014).
- Wang, Z., Alexandradinata, A., Cava, R. J. & Bernevig, B. A. Hourglass fermions. *Nature* **532**, 189–194 (2016).
- Wieder, B. J. et al. Wallpaper fermions and the nonsymmorphic Dirac insulator. *Science* **361**, 246–251 (2018).
- Po, H. C., Vishwanath, A. & Watanabe, H. Symmetry-based indicators of band topology in the 230 space groups. *Nat. Commun.* **8**, 50 (2017).
- Kruthoff, J., de Boer, J., van Wezel, J., Kane, C. L. & Slager, R.-J. Topological classification of crystalline insulators through band structure combinatorics. *Phys. Rev. X* **7**, 041069 (2017).
- Song, Z., Zhang, T., Fang, Z. & Fang, C. Quantitative mappings between symmetry and topology in solids. *Nat. Commun.* **9**, 3530 (2018).
- Khalaf, E., Po, H. C., Vishwanath, A. & Watanabe, H. Symmetry indicators and anomalous surface states of topological crystalline insulators. *Phys. Rev. X* **8**, 031070 (2018).
- Tang, F., Po, H. C., Vishwanath, A. & Wan, X. Comprehensive search for topological materials using symmetry indicators. *Nature* **566**, 486–489 (2019).
- Watanabe, H., Po, H. C. & Vishwanath, A. Structure and topology of band structures in the 1651 magnetic space groups. *Sci. Adv.* **4**, eaat8685 (2018).
- Hirschberger, M. et al. The chiral anomaly and thermopower of Weyl fermions in the half-Heusler  $\text{GdPtBi}$ . *Nat. Mater.* **15**, 1161–1165 (2016).
- Yang, H. et al. Topological Weyl semimetals in the chiral antiferromagnetic materials  $\text{Mn}_3\text{Ge}$  and  $\text{Mn}_3\text{Sn}$ . *New J. Phys.* **19**, 015008 (2017).
- Li, H. et al. Dirac surface states in intrinsic magnetic topological insulators  $\text{EuSn}_2\text{As}_2$  and  $\text{MnBi}_2\text{Te}_{2+n}$ . *Phys. Rev. X* **9**, 041039 (2019).
- Liu, D. F. et al. Magnetic Weyl semimetal phase in a kagomé crystal. *Science* **365**, 1282–1285 (2019).
- Belopolski, I. et al. Discovery of topological Weyl fermion lines and drumhead surface states in a room temperature magnet. *Science* **365**, 1278–1281 (2019).
- Zhang, D. et al. Topological axion states in the magnetic insulator  $\text{MnBi}_2\text{Te}_4$  with the quantized magnetoelectric effect. *Phys. Rev. Lett.* **122**, 206401 (2019).
- Soh, J.-R. et al. Ideal Weyl semimetal induced by magnetic exchange. *Phys. Rev. B* **100**, 201102 (2019).
- Nie, S., Xu, G., Prinz, F. B. & Zhang, S.-C. Topological semimetal in honeycomb lattice  $\text{LnSi}$ . *Proc. Natl Acad. Sci. USA* **114**, 10596–10600 (2017).
- Zou, J., He, Z. & Xu, G. The study of magnetic topological semimetals by first principles calculations. *npj Comput. Mater.* **5**, 1–19 (2019).
- Hua, G. et al. Dirac semimetal in type-IV magnetic space groups. *Phys. Rev. B* **98**, 201116 (2018).
- Shubnikov, A. V. Belov, N.V. & Holser, W.T. *Colored Symmetry* (Macmillan, 1964).
- Wieder, B. J. et al. Strong and fragile topological Dirac semimetals with higher-order Fermi arcs. *Nat. Commun.* **11**, 627 (2020).
- Xu, Y., Song, Z., Wang, Z., Weng, H. & Dai, X. Higher-order topology of the axion insulator  $\text{EuIn}_2\text{As}_2$ . *Phys. Rev. Lett.* **122**, 256402 (2019).
- Wieder, B. J. & Bernevig, B. A. The axion insulator as a pump of fragile topology. Preprint at <https://arxiv.org/abs/1810.02373> (2018).
- Fu, L. & Kane, C. L. Topological insulators with inversion symmetry. *Phys. Rev. B* **76**, 045302 (2007).
- Wilczek, F. Two applications of axion electrodynamics. *Phys. Rev. Lett.* **58**, 1799 (1987).
- Qi, X.-L., Hughes, T. L. & Zhang, S.-C. Topological field theory of time-reversal invariant insulators. *Phys. Rev. B* **78**, 195424 (2008).
- Mong, R. S. K., Essin, A. M. & Moore, J. E. Antiferromagnetic topological insulators. *Phys. Rev. B* **81**, 245209 (2010).
- Essin, A. M., Moore, J. E. & Vanderbilt, D. Magnetoelectric polarizability and axion electrodynamics in crystalline insulators. *Phys. Rev. Lett.* **102**, 146805 (2009).
- Hughes, T. L., Prodan, E. & Bernevig, B. A. Inversion-symmetric topological insulators. *Phys. Rev. B* **83**, 245132 (2011).
- Turner, A. M., Zhang, Y., Mong, R. S. K. & Vishwanath, A. Quantized response and topology of magnetic insulators with inversion symmetry. *Phys. Rev. B* **85**, 165120 (2012).
- Khalaf, E. Higher-order topological insulators and superconductors protected by inversion symmetry. *Phys. Rev. B* **97**, 205136 (2018).
- Li, C.-Z. et al. Reducing electronic transport dimension to topological hinge states by increasing geometry size of Dirac semimetal Josephson junctions. *Phys. Rev. Lett.* **124**, 156601 (2020).
- Morali, N. et al. Fermi-arc diversity on surface terminations of the magnetic Weyl semimetal  $\text{Co}_3\text{Sn}_2\text{S}_2$ . *Science* **365**, 1286–1291 (2019).
- Kuroda, K. et al. Evidence for magnetic Weyl fermions in a correlated metal. *Nat. Mater.* **16**, 1090 (2017).
- Varnava, N., Souza, I. & Vanderbilt, D. Axion coupling in the hybrid Wannier representation. *Phys. Rev. B* **101**, 155130 (2020).

**Publisher's note** Springer Nature remains neutral with regard to jurisdictional claims in published maps and institutional affiliations.

© The Author(s), under exclusive licence to Springer Nature Limited 2020

## Methods

### Concepts

Here we give a brief introduction to MTQC<sup>4,7,56–58</sup> and the definitions of six topological classes. A magnetic band structure below the Fermi level is partially described by the irreps formed by the occupied electronic states at the high-symmetry  $\mathbf{k}$  points, which are defined as the momenta whose little groups—the groups that leave the momenta unchanged—are maximal subgroups of the space group. If the highest occupied (valence) band and the lowest unoccupied (conduction) band are degenerate at a high-symmetry  $\mathbf{k}$  point, then we refer to the material as an enforced semimetal with Fermi degeneracy (ESFD)<sup>4</sup>. Depending on whether the irreps at high-symmetry points satisfy the so-called compatibility relations<sup>4,24,25,58</sup>—which determine whether the occupied bands must cross with unoccupied bands along high-symmetry lines or planes (whose little groups are non-maximal)—band structures can then be further classified as insulating (along high-symmetry lines and planes) or enforced semimetals. Materials classified as enforced semimetals generically feature band crossings along high-symmetry lines or planes. If a band structure satisfies the compatibility relations, it can be: (1) a trivial insulator, whose occupied bands form a band representation<sup>4</sup>; (2) a topological semimetal with crossing nodes at generic momenta (SISM) or non-symmetry-indicated topological semimetal, a system which satisfies all compatibility relations but exhibits Weyl-type nodes; or (3) a topological insulator. Some of the topological semimetals and insulators can be diagnosed through their irreps. If the irreps do not match a band representation, then the band structure must be a topological insulator or a SISM. There are two types of topological insulators: (1) stable topological insulators<sup>26,27,59,60</sup>, which include crystalline and higher-order topological insulators (topological crystalline insulators and HOTIs, respectively)<sup>61–65</sup>; and (2) fragile topological insulators<sup>60,66–70</sup>. Stable topological insulators remain topological when coupled to trivial or fragile bands, whereas fragile topological insulators, on the other hand, can be trivialized by being coupled to certain trivial bands, or even other fragile bands<sup>41,43</sup>. In ref. <sup>7</sup>, we explicitly identify all of the symmetry-indicated stable electronic (fermionic) topological insulators and topological semimetals, specifically detailing the bulk, surface, and hinge states of all symmetry-indicated stable topological insulators, topological crystalline insulators, and HOTIs in all 1651 spinful (double) magnetic and nonmagnetic space groups.

To summarize, using MTQC, we divide an electronic band structure into one of six topological classes—band representations, ESFD, enforced semimetal, SISM, stable topological insulator, and fragile topological insulator—of which only band representations are considered to be topologically trivial. If a band structure satisfies the compatibility relations along high-symmetry lines and planes, and has a nontrivial value of a stable index, then, unlike in the nonmagnetic space groups, it is possible for the bulk to be a topological (semi)metal<sup>7</sup>. We label these cases SISMs. See Supplementary Information section 1 for a more detailed description of the six topological classes.

### Magnetic materials database

We perform high-throughput calculations of the magnetic structures listed on BCSMD<sup>71</sup>. BCSMD contains portable structure files, including magnetic structure data and symmetry information, for 707 magnetic structures. The magnetic structures of all the materials are determined by neutron scattering experiments. We thus consider it reasonable and experimentally motivated to use the crystal and magnetic structures provided on the BCSMD as the initial inputs for ab initio calculations, instead of letting our theoretical ab initio codes predict the magnetic ground state. We emphasize that predictions of topological magnetic materials based on theoretically calculated magnetic structures, rather than experimentally measured structures, are more likely to predict unphysical (and possibly incorrect) magnetic ground states. From the 707 magnetic structures on the BCSMD, we omit 63 structures with

lattice-incommensurate magnetism and 95 alloys, as they do not have translation symmetry and hence are not invariant under any MSG. We apply ab initio calculations for the remaining 549 structures. These magnetic structures belong to 261 different MSGs, including 29 chiral MSGs and 232 achiral MSGs (chiral MSGs are defined as MSGs without improper rotations or combinations of improper rotations and time reversal; all other MSGs are achiral). In Supplementary Information section 2, we list the number of materials with experimentally obtained magnetic structures for each MSG.

### Calculation methods

We performed ab initio calculations incorporating spin–orbit coupling using VASP<sup>72</sup>. Because all of the magnetic materials on BCSMD with translation symmetry contain at least one correlated atom with 3*d*, 4*d*, 4*f* or 5*f* electrons, we apply a series of LDA + *U* calculations for each material with different Hubbard *U* parameters to obtain a full phase diagram. For all of the 3*d* valence orbitals and the atom Ru with 4*d* valence orbitals, we take *U* as 0 eV, 1 eV, 2 eV, 3 eV and 4 eV. The other atoms with 4*d* valence electrons usually do not exhibit magnetism or have weak correlation effects, and hence are not considered to be correlated in our calculations. Conversely, atoms with 4*f* and 5*f* valence electrons have stronger correlation effects, so we take *U* for atoms with 4*f* or 5*f* valence electrons to be 0 eV, 2 eV, 4 eV and 6 eV. If a material has both *d* and *f* electrons near the Fermi level, we fix the *U* parameter of the *d* electrons at 2 eV, and take *U* of the *f* electrons to be 0 eV, 2 eV, 4 eV and 6 eV sequentially. We also adopt four other exchange–correlation functionals in the LDA + *U* scheme to check the consistency between different functionals. Further details of our first-principles calculations are provided in Supplementary Information sections 3–6.

Of the 549 magnetic structures that we examined, 403 converged self-consistently to a magnetic ground state within an energy threshold of 10<sup>−5</sup> eV per cell. For 324 of the 403 converged materials, magnetic moments matching the experimental values (up to an average error of 50%) were obtained for at least one of the values of *U* used to obtain the material phase diagram. We stress that these are good agreements for calculations on these strongly correlated states. However, for the other 79 materials, the calculated magnetic momenta always notably diverged from the experimental values (see Supplementary Information section 12 for a complete comparison of the experimental and ab initio magnetic moments). The differences can be explained as follows. First, we consider only the spin components, but not the orbital components, of the magnetic moments in our current ab initio calculations. This can result in a large average error for compounds with large spin–orbital coupling. Second, because the average error is defined relative to the experimental moments, the ‘error’ (measured as a percentage) is likely to be larger when the experimental moments are small. In this case, the random, slight changes in the numerically calculated moments have an outsized effect on the reported error percentage. Last but not least, mean-field theory applied in the LDA + *U* calculations is not a good approximation for some strongly correlated materials, which should be checked further with more advanced methods. Although the prediction of magnetic structure with mean-field theory is sometimes not reliable for strongly correlated materials, it is worth comparing the energy difference between the magnetic structures from neutron scattering and the other possible magnetic structures. In Supplementary Information section 4, we selected several topological materials and compared their energies with some possible magnetic configurations and different *U*. We find that their experimental magnetic configurations have the lowest energies, and hence are theoretically favoured. Finally, we have additionally performed self-consistent calculations of the charge density at different values of *U*, which we used as input for our band structure calculations. In Supplementary Information section 13, we provide a complete summary of results.

Considering the possible underestimation of the band gap by generalized gradient approximations (GGA), the electronic structures of

23 topological materials are further confirmed by the calculations using the modified Becke–Johnson potential<sup>73</sup>. As shown in Supplementary Information section 5.2, both the features of bands near the Fermi level and the topological classes obtained from the Becke–Johnson potential are consistent with LDA +  $U$  calculations. Because of the limitations of the LDA +  $U$  method, we have also performed the more costly LDA + Gutzwiller<sup>74</sup> calculations in two of the topological materials identified in this work—CeCo<sub>2</sub>P<sub>2</sub> and MnGeO<sub>3</sub>, both classified as enforced semimetals—to confirm the bulk topology. As shown in Supplementary Information section 6, the strong correlations renormalize the quasiparticle spectrum by a factor of quasiparticle weight, but do not change the band topology. The surface-state calculations have been performed using the WannierTools package<sup>75</sup>.

### Identification of the magnetic irreps

Using the self-consistent charge density and potentials, we calculate the Bloch wavefunctions at the high-symmetry momenta in the Brillouin zone and then identify the corresponding magnetic irreps using the MagVasp2trace package, which is the magnetic version of Vasp2trace package<sup>76</sup>. (See Supplementary Information section 3 for details about MagVasp2trace.) The little group  $G_{\mathbf{k}}$  of a high-symmetry point  $\mathbf{k}$  is in general isomorphic to an MSG. For little groups without anti-unitary operations, we calculate the traces of the symmetry representations formed by the wavefunctions, and then decompose the traces into the characters of the small irreps of the little group  $G_{\mathbf{k}}$ . For little groups with anti-unitary operations, we calculate only the traces of the unitary operations and decompose the representations into the irreps of the maximal unitary subgroup  $G_{\mathbf{k}}^U$  of  $G_{\mathbf{k}}$ . Since anti-unitary operations in general lead to additional degeneracies, specifically enforcing two irreps of  $G_{\mathbf{k}}^U$  to become degenerate and form a co-representation, we check whether the additional degeneracies hold in the irreps obtained. Because VASP does not impose anti-unitary (magnetic) symmetries, degeneracies labelled by magnetic co-representations may exhibit very small splittings in band structures generated by VASP. In these cases, we reduce the convergence threshold and re-run the self-consistent calculation until the splitting is specifically small ( $\leq 10\%$ ) compared to the smallest energy gap across all of the high-symmetry momenta.

The algorithm and methods designed in this work are also applicable to future high-throughput searches for magnetic topological materials<sup>77</sup>.

### Details of the chemical categories

Considering the magnetic ions and chemical bonding of the magnetic materials, we classify the topological magnetic materials predicted in this work into the following 11 chemical categories.

**I-A.** Non-collinear manganese compounds, which have received considerable recent attention owing to their unusual combination of a large anomalous Hall effect and net-zero magnetic moments. The symmetry of the non-collinear antiferromagnet spin structure allows for a non-vanishing Berry curvature, the origin of the unusual anomalous Hall effect. Examples of non-collinear manganese compounds include the hexagonal Weyl semimetals Mn<sub>3</sub>Sn, Mn<sub>3</sub>Ge and the well-studied cubic antiferromagnetic spintronic material Mn<sub>3</sub>Ir, as well as the inverse perovskite compounds Mn<sub>3</sub>YZ, which represent ‘stuffed’ versions of the cubic Mn<sub>3</sub>Y compounds.

**I-B and I-C.** Intermetallic materials, containing rare-earth atoms or actinide atoms, which are typically antiferromagnets. The variation of the Hubbard  $U$  changes the band structures slightly in these materials, but not the topological character.

**II-A.** The ThCr<sub>2</sub>Si<sub>2</sub> structure and related structures, which have received attention because of the high-temperature iron pnictide

superconductors in this group. In these materials, the transition-metal layers and the pnictide layers form square lattices. The square nets of the pnictides act as a driving force for a topological band structure<sup>78</sup>. Several of the antiferromagnetic undoped prototypes, such as CaFe<sub>2</sub>As<sub>2</sub>, are topological antiferromagnets. This suggests the possibility of topological superconductivity in these materials, like that recently found in FeTe<sub>0.55</sub>Se<sub>0.45</sub> (ref. <sup>79</sup>).

**II-B.** Semiconducting manganese pnictines, which occur when iron is substituted with manganese, leading to materials that are trivial when insulating and gapped, but which become topological antiferromagnets when their gap is closed. By increasing the Hubbard  $U$ , the antiferromagnetic phases of these compounds can be converted into trivial insulators. The antiferromagnetic insulators and semimetals in this class can also be converted into ferromagnetic metals by doping.

**II-C.** Transition metals in combination with rare-earth or actinide atoms form compounds of the ThCr<sub>2</sub>Si<sub>2</sub> structure type. Here the antiferromagnetic ordering comes from the thorium position in the ThCr<sub>2</sub>Si<sub>2</sub> structure type.

**I-D.** Rare-earth ternary compounds of the composition 1:1:1.

**III-A, III-B, III-C and III-D.** The third class of magnetic materials are ionic compounds, of which most have been experimentally determined to be insulating. Within the density functional approximation, several of the compounds have been identified as topological nontrivial metals, such as oxides, borates, hydroxides, silicates, phosphates and FeI<sub>2</sub>. By increasing the Hubbard  $U$ , a topologically trivial gap can be opened in these materials.

Additional data and discussion can be found in the Supplementary Information.

### Data availability

All data are available in the Supplementary Information and at <https://www.topologicalquantumchemistry.fr/magnetic>. The codes required to calculate the character table of magnetic materials are available at <https://www.cryst.ehu.es/cryst/checktopologicalmagmat>.

56. Elcoro, L. et al. Double crystallographic groups and their representations on the Bilbao Crystallographic Server. *J. Appl. Cryst.* **50**, 1457–1477 (2017).
57. Cano, J. et al. Building blocks of topological quantum chemistry: elementary band representations. *Phys. Rev. B* **97**, 035139 (2018).
58. Vergniory, M. G. et al. Graph theory data for topological quantum chemistry. *Phys. Rev. E* **96**, 023310 (2017).
59. Song, Z., Huang, S.-J., Qi, Y., Fang, C. & Hermele, M. Topological states from topological crystals. *Sci. Adv.* **5**, eaax2007 (2019).
60. Elcoro, L., Song, Z. & Bernevig, B. A. Application of induction procedure and smith decomposition in calculation and topological classification of electronic band structures in the 230 space groups. *Phys. Rev. B* **102**, 035110 (2020).
61. Benalcazar, W. A., Bernevig, B. A. & Hughes, T. L. Quantized electric multipole insulators. *Science* **357**, 61–66 (2017).
62. Schindler, F. et al. Higher-order topological insulators. *Sci. Adv.* **4**, eaat0346 (2018).
63. Schindler, F. et al. Higher-order topology in bismuth. *Nat. Phys.* **14**, 918–924 (2018).
64. Song, Z., Fang, Z. & Fang, C. ( $d-2$ )-dimensional edge states of rotation symmetry protected topological states. *Phys. Rev. Lett.* **119**, 246402 (2017).
65. Langbehn, J., Peng, Y., Trifunovic, L., von Oppen, F. & Brouwer, P. W. Reflection-symmetric second-order topological insulators and superconductors. *Phys. Rev. Lett.* **119**, 246401 (2017).
66. Po, H. C., Watanabe, H. & Vishwanath, A. Fragile topology and Wannier obstructions. *Phys. Rev. Lett.* **121**, 126402 (2018).
67. Cano, J. et al. Topology of disconnected elementary band representations. *Phys. Rev. Lett.* **120**, 266401 (2018).
68. Bradlyn, B., Wang, Z., Cano, J. & Bernevig, B. A. Disconnected elementary band representations, fragile topology, and Wilson loops as topological indices: an example on the triangular lattice. *Phys. Rev. B* **99**, 045140 (2019).
69. Ahn, J., Park, S. & Yang, B.-J. Failure of Nielsen–Ninomiya theorem and fragile topology in two-dimensional systems with space-time inversion symmetry: application to twisted bilayer graphene at magic angle. *Phys. Rev. X* **9**, 021013 (2019).



70. Song, Z.-D., Elcoro, L., Xu, Y.-F., Regnault, N. & Bernevig, B. A. Fragile phases as affine monoids: classification and material examples. *Phys. Rev. X* **10**, 031001 (2020).
71. Gallego, S. V. et al. MAGNDATA: towards a database of magnetic structures. I. The commensurate case. *J. Appl. Cryst.* **49**, 1750–1776 (2016).
72. Kresse, G. & Furthmüller, J. Efficient iterative schemes for ab initio total-energy calculations using a plane-wave basis set. *Phys. Rev. B* **54**, 11169–11186 (1996).
73. Tran, F. & Blaha, P. Accurate band gaps of semiconductors and insulators with a semilocal exchange-correlation potential. *Phys. Rev. Lett.* **102**, 226401 (2009).
74. Deng, X. Y., Wang, L., Dai, X. & Fang, Z. Local density approximation combined with Gutzwiller method for correlated electron systems: formalism and applications. *Phys. Rev. B* **79**, 075114 (2009).
75. Wu, Q.S., Zhang, S. N., Song, H.-F., Troyer, M. & Soluyanov, A. A. WannierTools: an open-source software package for novel topological materials. *Comp. Phys. Commun.* **224**, 405–416 (2018).
76. Gao, J., Wu, Q., Persson, C. & Wang, Z. Irvsp: to obtain irreducible representations of electronic states in the VASP. Preprint at <https://arxiv.org/abs/2002.04032> (2020).
77. Frey, N. C. et al. High-throughput search for magnetic and topological order in transition metal oxides. Preprint at <https://arxiv.org/abs/2006.01075> (2020).
78. Xu, Q. et al. Two-dimensional oxide topological insulator with iron-pnictide superconductor LiFeAs structure. *Phys. Rev. B* **92**, 205310 (2015).
79. Wang, D. et al. Evidence for Majorana bound states in an iron-based superconductor. *Science* **362**, 333–335 (2018).

**Acknowledgements** We thank U. Schmidt, I. Weidl, W. Shi and Y. Zhang. We acknowledge the computational resources Cobra in the Max Planck Computing and Data Facility (MPCDF), the HPC Platform of ShanghaiTech University and Atlas in the Donostia International Physics Center (DIPC). Y.X. is grateful to D. Liu for help in plotting some diagrammatic sketches. B.A.B., N.R., B.J.W. and Z.S. were primarily supported by a Department of Energy grant (DE-SC0016239), and partially supported by the National Science Foundation (EAGER grant DMR 1643312), a Simons Investigator grant (404513), the Office of Naval Research (ONR; grant N00014-14-1-0330), the NSF-MRSEC (grant DMR-142051), the Packard Foundation, the Schmidt

Fund for Innovative Research, the BSF Israel US foundation (grant 2018226), the ONR (grant N00014-20-1-2303) and a Guggenheim Fellowship (to B.A.B.). Additional support was provided by the Gordon and Betty Moore Foundation through grant GBMF8685 towards the Princeton theory programme. L.E. was supported by the Government of the Basque Country (Project IT1301-19) and the Spanish Ministry of Science and Innovation (PID2019-106644GB-I00). M.G.V. acknowledges support from the Diputacion Foral de Gipuzkoa (DFG; grant INCEN2019-000356) from Gipuzkoako Foru Aldundia and the Spanish Ministerio de Ciencia e Innovación (grant PID2019-109905GB-C21). Y.C. was supported by the Shanghai Municipal Science and Technology Major Project (grant 2018SHZDX02) and a Engineering and Physical Sciences Research Council (UK) Platform Grant (grant EP/M020517/1). C.F. acknowledges financial support by the DFG under Germany's Excellence Strategy through the Würzburg-Dresden Cluster of Excellence on Complexity and Topology in Quantum Matter (ct.qmat EXC 2147, project-id 390858490), an ERC Advanced Grant (742068 'TOPMAT'). Y.X. and B.A.B. were also supported by the Max Planck Society.

**Author contributions** B.A.B. conceived this work; Y.X. and M.G.V. performed the first-principles calculations. L.E. wrote the code for calculating the irreducible representations and checking the topologies of materials. Y.X., Z.S., B.J.W. and B.A.B. analysed the calculated results, B.J.W. determined the physical meaning of the topological indices with help from L.E., Z.S. and Y.X. C.F. performed chemical analysis of the magnetic topological materials. N.R. built the topological material database. All authors wrote the main text and Y.X. and Z.S. wrote the Methods and the Supplementary Information.

**Competing interests** The authors declare no competing interests.

## Additional information

**Supplementary information** is available for this paper at <https://doi.org/10.1038/s41586-020-2837-0>.

**Correspondence and requests for materials** should be addressed to B.A.B.

**Peer review information** *Nature* thanks the anonymous reviewers for their contribution to the peer review of this work.

**Reprints and permissions information** is available at <http://www.nature.com/reprints>.